Highlights in High-Energy Physics
https://www.sciltp.com/journals/hihep

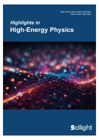

Article

Hadronic Decay Branching Ratio Measurements of the Higgs Boson at Future Colliders Using the Holistic Approach

Jianfeng Jiang [1,2], Yongfeng Zhu [1], Chao Yang [1,2] and Manqi Ruan [1,*]

[1] Institute of High Energy Physics, Chinese Academy of Sciences, Beijing 100049, China
[2] University of Chinese Academy of Sciences, Beijing 100049, China
* Correspondence: manqi.ruan@ihep.ac.cn

How To Cite: Jiang, J.; Zhu, Y.; Yang, C.; et al. Hadronic Decay Branching Ratio Measurements of the Higgs Boson at Future Colliders Using the Holistic Approach. *Highlights in High-Energy Physics* **2026**, *2*(1), 5. https://doi.org/10.53941/hihep.2026.100005

Received: 6 March 2026
Revised: 25 March 2026
Accepted: 27 March 2026
Published: 31 March 2026

Abstract: Accurately measuring the properties of the Higgs boson is one of the primary physics objectives of the high-energy frontier. By incorporating the inclusive information of all reconstructed particles to identify the signal events, referred to as the holistic approach, we estimate the relative statistical uncertainty for the Higgs hadronic decay modes $H \to b\bar{b}$, $c\bar{c}$, gg, $WW^* \to 4q$, and $ZZ^* \to 4q$ at the Circular Electron–Positron Collider (CEPC) operating as a Higgs factory with an integrated luminosity of 21.6 ab^{-1}. In the $Z(\mu^+\mu^-)H$ and $Z(\nu\overline{\nu})H$ channels, the relative statistical uncertainties for these decay modes are projected to range from 0.36% to 5.21% and 0.16% to 2.52%, respectively. Compared to the CEPC Snowmass results, the holistic approach boosts the measurement precision by a factor of two to four. The scaling behavior, specifically the dependence of the anticipated accuracy on the training dataset size, is observed and analyzed. The precision of these leading Higgs decay modes, especially the $H \to b\bar{b}$ mode, is asymptotically approaching the statistical limit. The scaling behavior could also be applied to monitor the robustness and to quantify the uncertainties of the holistic approach.

Keywords: higgs; artificial intelligence; scaling law

1. Introduction

After the discovery of the Higgs boson at the Large Hadron Collider (LHC) in 2012 [1,2], a primary objective of high-energy physics has been the search for new physics via the Higgs portal, especially through the precise measurement of the Higgs boson couplings. The hadronic decays of the Higgs boson account for a cumulative branching ratio of approximately 80%, making them critical for precise Higgs property measurements. Those measurements at the LHC are significantly limited due to the overwhelming QCD backgrounds and severe pile-up conditions. Meanwhile, identified as the highest-priority future collider facility [3,4], the electron-positron Higgs factory offers a clean collision environment ideal for exploring these hadronic decay modes. Prominent proposals include the Circular Electron–Positron Collider (CEPC) [5–8], the Future Circular Collider (FCC-ee) [9], the International Linear Collider (ILC) [10], the Compact Linear Collider (CLIC) [11] and many others such as LEP3 [12].

Artificial intelligence (AI) has significantly advanced data analysis techniques in high-energy physics [13]. Jet origin identification (JOI) [14] classifies jets according to their underlying parton flavor, while one-to-one reconstruction techniques [15] associate detector hits with individual reconstructed particles to identify their species. More recently, an Advanced Color-Singlet Identification (ACSI) algorithm [16] has been developed to directly associate final-state particles with their parent bosons.

To exploit the physics potential of the electron-positron Higgs factory, we adopt the holistic approach to the measurements of leading Higgs hadronic decay modes. The holistic approach is an end-to-end process that treats each collision event as an ensemble of reconstructed particles, it reads in the inclusive particle-level information and infers the event type according to its training. By utilizing high-dimensional input data, this approach incorporates approximately two orders of magnitude more input information compared to traditional method (Traditional Higgs measurements usually rely on cut-based analyses with $\mathcal{O}(10)$ discriminating variables, such as in $H \to b\bar{b}/c\bar{c}/gg$ studies [17]. In contrast, the holistic approach directly uses particle-level information (e.g., four-momentum, impact parameters, and particle type), corresponding to about ten features per particle. For events with approximately 100 reconstructed particles, this results in thousands of input features). We also observe the scaling behavior, which describes the evolution of performance with changing training data size. The scaling behavior is then applied to the analysis optimization, AI model behavior monitoring, and uncertainty control.

This paper is organized as follows: Section 2 introduces the detector model, software framework, AI algorithm, and simulated data samples used in this analysis. Section 3 presents the analyses in the $Z(\mu^+\mu^-)H$ and $Z(\nu\bar{\nu})H$ channels and the extrapolated results. Section 4 discusses the observed scaling behavior and the generator robustness of the holistic approach. Section 5 provides a summary and outlook.

2. Detector, Samples, and Methods

This study is based on the CEPC operating as a Higgs factory at a center-of-mass energy of 240 GeV, using the AURORA detector model [15]. AURORA is a particle-flow–oriented detector design evolved from the CEPC Conceptual Design Report (CDR) baseline detector [6]. It features high-granularity electromagnetic and hadronic calorimeters (ECAL and HCAL), a high-precision tracking system with a low material budget, a high-resolution vertex detector, and a large solenoidal magnet enclosing the calorimeters. In addition, both ECAL and HCAL are assumed to provide a per-cell time resolution of $O(100)$ ps. The critical performance of AURORA is summarized in Figure 1. AURORA achieves a Boson Mass Resolution (BMR) (BMR is defined as the relative invariant-mass resolution for hadronically decaying heavy bosons (Z, W, and Higgs bosons), and is a key performance metric for Higgs factory detectors.) of 2.7%, which is a critical figure of merit representing the relative uncertainties on the reconstructed invariant mass of heavy bosons especially the Higgs boson. Equipped with high-precision and high-granularity 5D calorimetry, AURORA offers efficient identification of the reconstructed particles, 97–100% simultaneous efficiencies for charged particles and photons, and 75–80% for neutral hadrons.

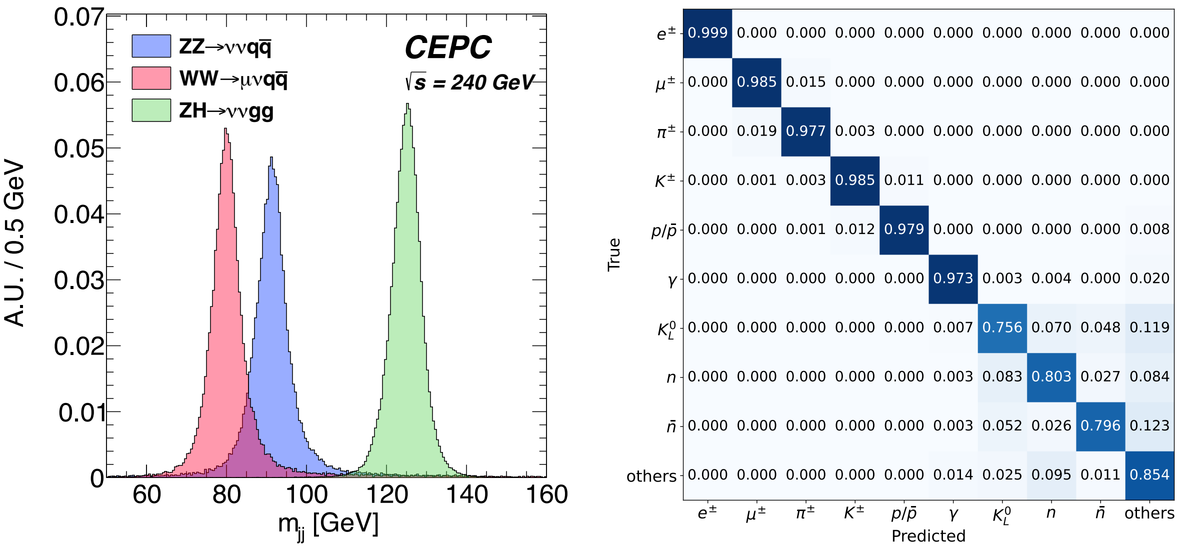

	$e^\pm$	$\mu^\pm$	$\pi^\pm$	$K^\pm$	$p/\bar{p}$	γ	K_L^0	n	$\bar{n}$	others
$e^\pm$	0.999	0.000	0.000	0.000	0.000	0.000	0.000	0.000	0.000	0.000
$\mu^\pm$	0.000	0.985	0.015	0.000	0.000	0.000	0.000	0.000	0.000	0.000
$\pi^\pm$	0.000	0.019	0.977	0.003	0.000	0.000	0.000	0.000	0.000	0.000
$K^\pm$	0.000	0.001	0.003	0.985	0.011	0.000	0.000	0.000	0.000	0.000
$p/\bar{p}$	0.000	0.000	0.001	0.012	0.979	0.000	0.000	0.000	0.000	0.008
γ	0.000	0.000	0.000	0.000	0.000	0.973	0.003	0.004	0.000	0.020
K_L^0	0.000	0.000	0.000	0.000	0.000	0.007	0.756	0.070	0.048	0.119
n	0.000	0.000	0.000	0.000	0.000	0.003	0.083	0.803	0.027	0.084
$\bar{n}$	0.000	0.000	0.000	0.000	0.000	0.003	0.052	0.026	0.796	0.123
others	0.000	0.000	0.000	0.000	0.000	0.014	0.025	0.095	0.011	0.854

Figure 1. Overview of the AURORA detector performance. **Left**: The reconstructed invariant mass distributions for hadronic systems in $WW \to \mu\nu q\bar{q}$, $ZZ \to \nu\nu q\bar{q}$, and $ZH \to \nu\nu gg$ processes at $\sqrt{s} = 240$ GeV. **Right**: Migration matrix for particle identification (PID) reconstruction, illustrating the identification efficiency for charged particles, photons, and neutral hadrons. The detector concept achieves near-universal particle identification performance.

The signal samples, including $Z(\mu^+\mu^-)H$ and $Z(\nu\bar{\nu})H$ with the Higgs boson decaying into five dominant hadronic modes ($H \to b\bar{b}$, $c\bar{c}$, gg, WW^*, ZZ^*), as well as the dominant Standard Model background processes ($e^+e^- \to ZZ$, WW, and $q\bar{q}$), were generated at Leading Order (LO) using MadGraph5_aMC@NLO [18]. The `isronlyll` parameterization [19] was employed to simulate Initial State Radiation (ISR), incorporating Leading-Logarithmic (LL) QED electron structure functions (PDFs) to model collinear photon radiation. Parton showering and hadronization were simulated with Pythia8 [20] using the default Monash 2013 tune. To ensure consistency and avoid double-counting, ISR generation in Pythia8 was disabled, given that these effects were already treated by the matrix element generator. Additionally, multi-parton interactions (MPI) were turned off, reflecting the clean nature of electron-positron collisions. Using the fast simulation tool Delphes [21], we mimic the performance of the AURORA detector [15], which features a BMR of approximately 3% and ideal particle identification (PID) for charged particles. The cross sections and expected event yields for all signal and background processes, normalized to an integrated luminosity of $21.6\ \mathrm{ab}^{-1}$, are summarized in Table 1.

Table 1. Expected yields and cross section(×BR) for $Z(\mu^+\mu^-)H$, $Z(\nu\bar{\nu})H$ and main background processes at 240 GeV center-of-mass energy with an integrated luminosity of $21.6\ \mathrm{ab}^{-1}$.

Channel	**Cross Section (× BR) [fb]**	**Expected Yield ($21.6\ \mathrm{ab}^{-1}$)**
$Z(\mu^+\mu^-)H(b\bar{b})$	3.8	8.3×10^4
$Z(\mu^+\mu^-)H(c\bar{c})$	0.19	4.2×10^3
$Z(\mu^+\mu^-)H(gg)$	0.57	1.2×10^4
$Z(\mu^+\mu^-)H(WW^*)$	0.65	1.4×10^4
$Z(\mu^+\mu^-)H(ZZ^*)$	0.086	1.8×10^3
$Z(\mu^+\mu^-)Z(q\bar{q})$	51	1.1×10^6
$Z(\nu\bar{\nu})H(b\bar{b})$	23	4.9×10^5
$Z(\nu\bar{\nu})H(c\bar{c})$	1.2	2.5×10^4
$Z(\nu\bar{\nu})H(gg)$	3.4	7.3×10^4
$Z(\nu\bar{\nu})H(WW^*)$	3.8	8.3×10^4
$Z(\nu\bar{\nu})H(ZZ^*)$	0.51	1.1×10^4
$W(l\nu)W(q\bar{q})$	1200	2.6×10^7
$Z(\nu\bar{\nu})Z(q\bar{q})$	150	3.2×10^6
$q\bar{q}$	54,000	1.2×10^{10}

The holistic approach can be realized using different deep learning architectures. In this work, it is implemented with ParticleNet(PN) [22], whose core building block is the EdgeConv operation that aggregates features from each particle and its k nearest neighbors. By stacking multiple EdgeConv blocks, the network performs message passing to learn local and global correlations, enabling the extraction of high-level representations directly from the particle cloud. The EdgeConv layers are followed by a channel-wise global average pooling layer and two fully connected layers, with a softmax activation used to produce event-level classification scores. The input features provided to the network encode comprehensive information from reconstructed particles, including:

- *Geometric coordinates*: The angular variables $\Delta\eta$ and $\Delta\phi$, defined relative to a reference axis. (To explicitly capture the global topology of the ZH process, a reference axis is introduced for coordinate transformation. For the $\mu^+\mu^-H$ channel, the reference axis is defined by the recoil system (the Higgs candidate), $p_{\text{recoil}} = p_{\text{initial}} - p_{\mu\mu}$. For the $\nu\bar{\nu}H$ channel, it is defined by the missing momentum vector (the Z boson candidate), $p_{\text{missing}} = p_{\text{initial}} - p_{\text{visible}}$. These coordinates are used to construct the dynamic k-nearest-neighbor graph).
- *Kinematic variables*: The transverse momentum (p_T) and energy (E), together with their normalized fractions ($p_T/p_{T,\text{evt}}$ and E/E_{evt}). The angular distance $\Delta R = \sqrt{\Delta\eta^2 + \Delta\phi^2}$ and the particle charge are also included.
- *Impact parameters*: The transverse (d_0) and longitudinal (d_z) impact parameters of the track, which are essential for resolving displaced vertices from heavy-flavor (b and c) decays.
- *Particle identification*: One-hot encoded labels (One-hot encoding is commonly used in artificial intelligence to represent categorical variables. In this representation, each label is expressed as a binary vector in which the element corresponding to the true particle class is set to 1, while all other elements are set to 0.) for the seven reconstructed particle species: $\mu^\pm, e^\pm, \gamma, \pi^\pm, K^\pm, p^\pm$, and neutral hadrons.

The output of the network consists of a set of event-level classification scores, normalized via a softmax function, representing the probability of the event belonging to each signal or background category.

For the $\mu^+\mu^-H$ channel, the model is trained on a dataset of 10^6 events. A separate validation dataset of 2×10^5 events is employed for hyperparameter tuning and model checkpointing to mitigate overfitting. The final performance metrics are evaluated on an independent inference dataset of 8×10^5 events, ensuring the statistical robustness of the results. For the $\nu\bar{\nu}H$ channel, the model is trained on a dataset of $10^5 \sim 10^6$ events, with 2×10^4 events allocated for validation and an independent inference dataset of 2×10^4 events. For both channels, the training process is carried out over 30 epochs.

3. Higgs Hadronic Decay Measurements

For the measurement of different Higgs decay processes in $\mu^+\mu^-H$ and $\nu\bar{\nu}H$ channels, we use the relative statistical uncertainty to evaluate the measurement performance. The relative statistical uncertainty is calculated as $\Delta\mu/\mu = \sqrt{S+B}/S$, where S and B denote the expected signal and background yields surviving the selection, respectively.

3.1. $\mu^+\mu^-H$ Channel

In the $\mu^+\mu^-H$ channel, the presence of two high-momentum muons allows for strong suppression of Standard Model backgrounds. However, the semileptonic ZZ production remains the dominant background source [23]. We apply the holistic approach to directly discriminate among the different Higgs decay processes and the semileptonic ZZ background. A training dataset of 10^6 events is used for each process in a multi-class classification setup.

The holistic approach takes the inclusive reconstructed particles as input, with a total dimensionality easily exceeding 10^3, and simultaneously infers the probability scores for all different event types. By assigning each event to the category with the highest inferred score, we construct the migration matrix shown in Figure 2. Each row represents the truth-level process, while each column corresponds to the model's prediction, with each row normalized to unity. The diagonal elements represent the correct classification efficiencies. A pronounced diagonal and symmetric (The migration matrices in Figure 2 are symmetric except for the misidentification between $H \to WW^*$ and $H \to ZZ^*$, where $P(ZZ \to WW)$ is roughly two times larger than $P(WW \to ZZ)$. A plausible explanation of this phenomenon is the flavor structure of $H \to WW^*/ZZ^* \to 4q$ decay, as roughly half of the $H \to ZZ^* \to 4q$ has b-quarks while $H \to WW^*$ has almost no b-quark in the $4q$ final states. This phenomenon is also observed in studies [13,23].) structure is observed. The model exhibits strong performance on topologically distinct signatures. The dominant Standard Model background, $Z(\mu^+\mu^-)Z(q\bar{q})$, achieves a high classification efficiency of over 99%, indicating that it can be effectively suppressed in event selection. The Higgs decay processes achieve the highest efficiency of 93.4% for the $H \to b\bar{b}$ channel, followed by 90.0% $H \to c\bar{c}$ and 84.4% for $H \to gg$. The off-diagonal elements quantify the misidentification rates among different channels. Similar behavior is also observed in the migration of the $\mu^+\mu^-H$ channel.

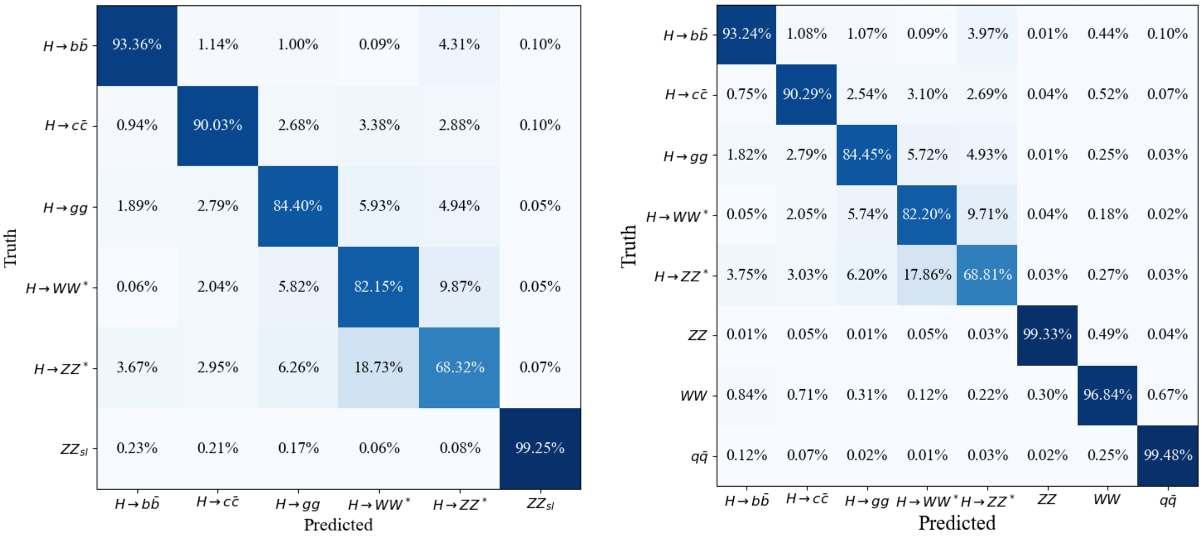

Figure 2. Migration matrix for the $\mu^+\mu^-H$ (**left**) and $\nu\bar{\nu}H$ (**right**) classification task using the holistic approach, trained on 1 M events. Matrix elements are normalized to unity in each row.

To extract the signal and evaluate the measurement precision for each specific decay mode, we scan the threshold on its corresponding classification score. The optimal working point is determined by maximizing the product of signal efficiency and purity. The relative statistical uncertainty, as defined at the beginning of this section, is calculated at this optimized cut value. Figure 3 presents the best cut and the score distribution for the Higgs decay modes. Depending on the signal topology and background contamination, the optimal thresholds vary significantly. The $H \to b\bar{b}$ process requires only a loose threshold (score > 0.11), whereas the $H \to c\bar{c}$ process demands a strict cut (score > 0.90) to effectively suppress the background. The optimized statistical uncertainties are 0.36% for $H \to b\bar{b}$, 2.14% for $H \to c\bar{c}$, 1.14% for $H \to gg$ and 0.99% for $H \to WW^*$.

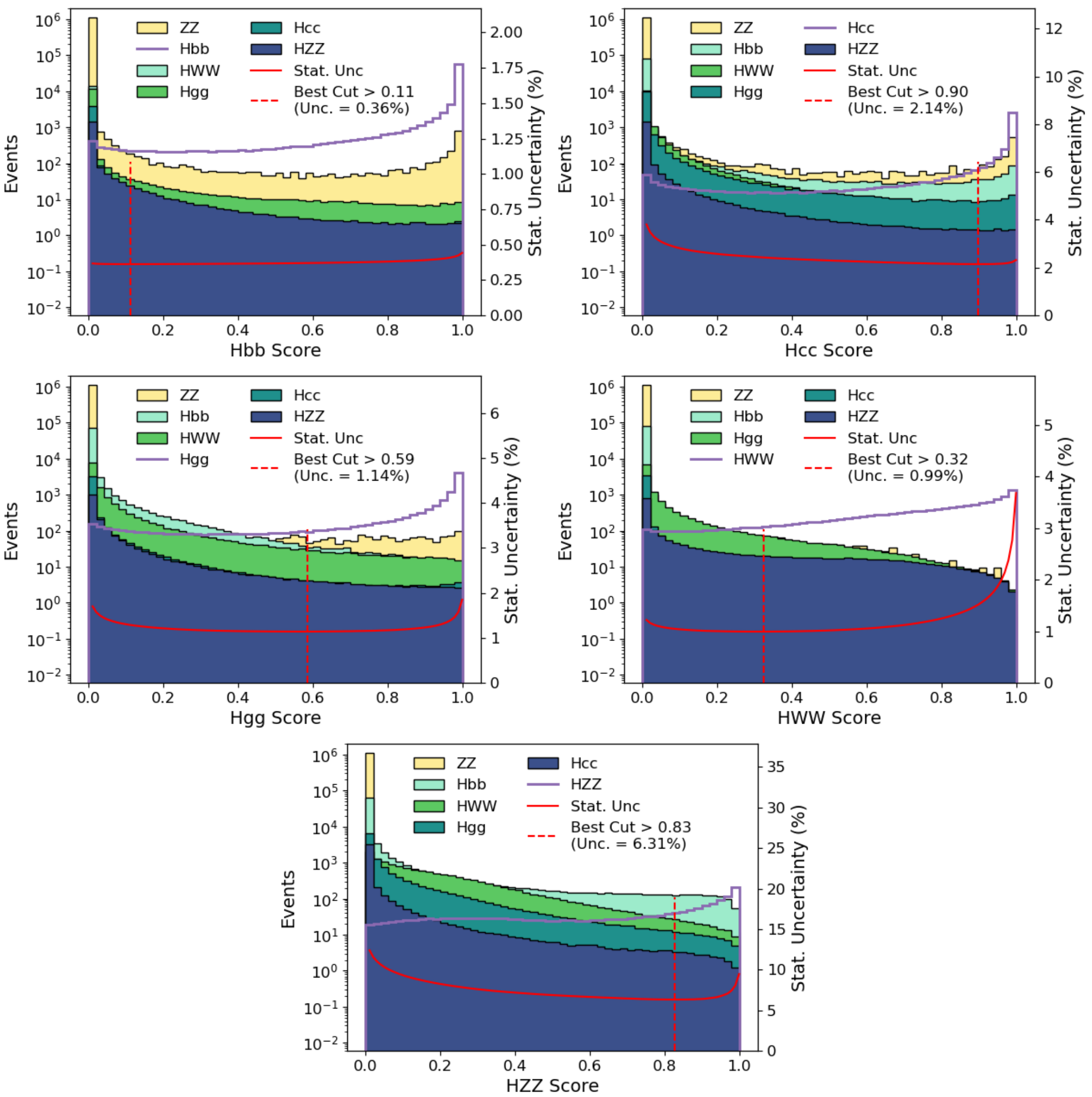

Figure 3. Score distributions and relative statistical uncertainties for $H \to b\bar{b}$, $H \to c\bar{c}$, $H \to gg$, $H \to WW^*$, and $H \to ZZ^*$ processes in the $\mu^+\mu^- H$ analysis using the holistic approach trained on 1 M events. The purple curve denotes the signal, while the colored histograms show the backgrounds. The red solid curve gives the statistical uncertainty versus the score cut, and the vertical red dashed line marks the optimal score cut.

For the $H \to ZZ^*$ channel, an anticipated relative statistical uncertainty of 6.31% is achieved. To fully exploit the classification information, we implemented a categorization strategy. $H \to b\bar{b}$ and $H \to WW^*$ are the primary backgrounds for the $H \to ZZ^*$ channel, we categorized the candidate events into four independent regions based on their inferred background scores and applied the optimal cut within each region. The detailed methodology is presented in Appendix A.

This categorization strategy yields an approximate 20% improvement for the $H \to ZZ^*$ measurement. We also applied this binned score method to the other hadronic decay processes. Table 2 summarizes the projected statistical uncertainties before and after this optimization, alongside their respective statistical limits.

Table 2. Projected relative statistical precision for the Higgs hadronic decay processes in the $Z(\mu^+\mu^-)H$ channel with an integrated luminosity of 21.6 ab^{-1}. The table compares the results from the optimal score cut and the binned optimal score cut against the statistical limits.

Processes	$H \to b\bar{b}$	$H \to c\bar{c}$	$H \to gg$	$H \to WW^*$	$H \to ZZ^*$
Score cut	0.36%	2.14%	1.14%	0.99%	6.31%
Binned score cut	0.36%	1.99%	1.08%	0.96%	5.21%
Stat. limit	0.35%	1.55%	0.90%	0.85%	2.33%

3.2. $\nu\bar{\nu}H$ Channel

For the $\nu\bar{\nu}H$ channel, the classification performance exhibits a pattern highly similar to that of the $\mu^+\mu^-H$ analysis, as shown in the migration matrix (Figure 2). While the migration matrix shows decent separation power, the background cross sections in the $\nu\bar{\nu}H$ channel remain significantly large. The expected yield of the $q\bar{q}$ background alone exceeds 10^{10} events, dwarfing the signal by several orders of magnitude, see Table 1. To mitigate this immense background contamination, a pre-selection based on kinematic variables is applied, see Table 3. At the cost of 5–20% of signal efficiency, this pre-selection suppresses the SM backgrounds by nearly three orders of magnitude.

Table 3. The cut flow of pre-selection, normalized to an integrated luminosity of 21.6 ab^{-1} at 240 GeV. M_{miss} and M_{inv} represent the total missing mass and the invariant mass of all visible particles, respectively, while the last column shows the overall pre-selection efficiency.

Channel	**Expected Events**	$p_{T,evt} > 10$ **GeV**	$60 < M_{miss} < 140$ **GeV**	$105 < M_{inv} < 160$ **GeV**	**Eff (%)**
$Z(\nu\bar{\nu})H(b\bar{b})$	4.9×10^5	4.77×10^5	4.63×10^5	3.93×10^5	80.20
$Z(\nu\bar{\nu})H(c\bar{c})$	2.5×10^4	2.41×10^4	2.38×10^4	2.20×10^4	89.29
$Z(\nu\bar{\nu})H(gg)$	7.3×10^4	7.13×10^4	7.08×10^4	6.94×10^4	95.30
$Z(\nu\bar{\nu})H(WW^*)$	8.3×10^4	8.12×10^4	8.08×10^4	7.91×10^4	95.08
$Z(\nu\bar{\nu})H(ZZ^*)$	1.1×10^4	1.07×10^4	1.06×10^4	1.01×10^4	92.09
$W(l\nu)W(q\bar{q})$	2.6×10^7	2.52×10^7	5.84×10^6	3.73×10^6	14.12
$Z(\nu\bar{\nu})Z(q\bar{q})$	3.2×10^6	3.18×10^6	3.00×10^6	5.99×10^4	1.83
$q\bar{q}$	1.2×10^{10}	6.47×10^8	4.56×10^8	1.63×10^7	0.14

Using the same architecture, another model is trained on the events passing the pre-selection, with 10^5 events to each category. Figure 4 presents the inferred score distributions for the five Higgs decay processes. Adopting the same method to the $\mu^+\mu^-H$ channel, we determine the optimal score threshold by maximizing the product of signal efficiency and purity. Applying these cuts yields projected relative statistical uncertainties of 0.17% for $H \to b\bar{b}$, 0.99% for $H \to c\bar{c}$, 0.48% for $H \to gg$, 0.45% for $H \to WW^*$ and 3.26% for $H \to ZZ^*$. By implementing the categorization strategy, these uncertainties are further refined to 0.17%, 0.94%, 0.47%, 0.43%, and 2.76%, respectively.

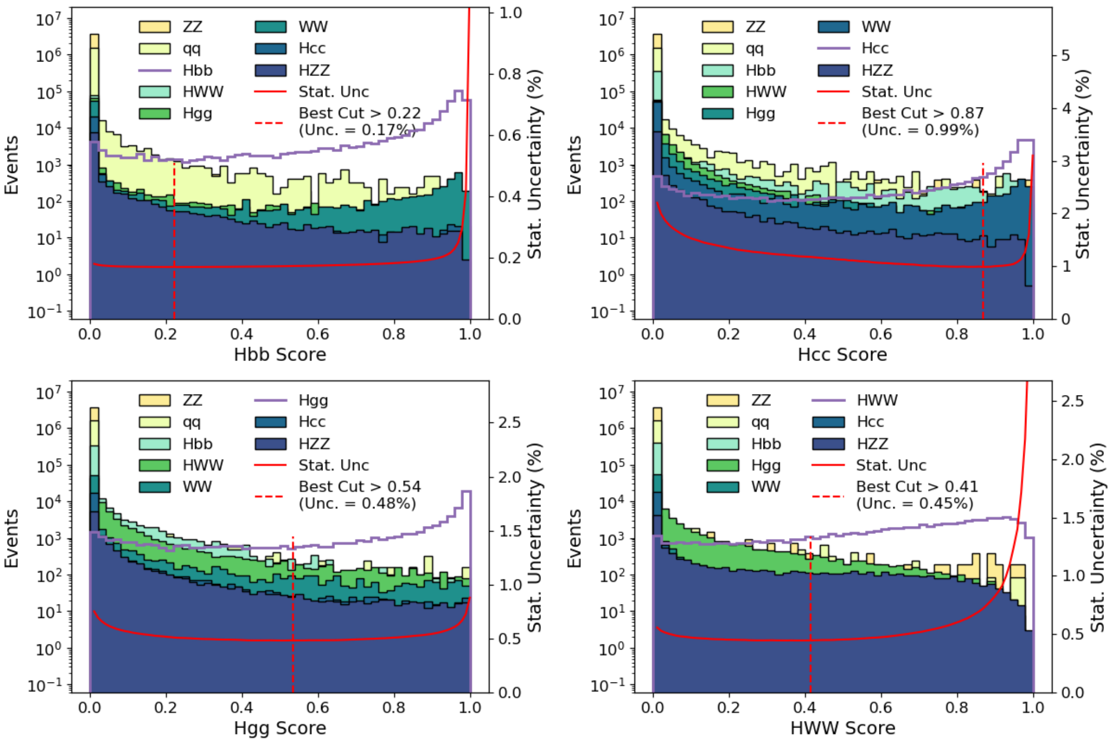

Figure 4. *Cont.*

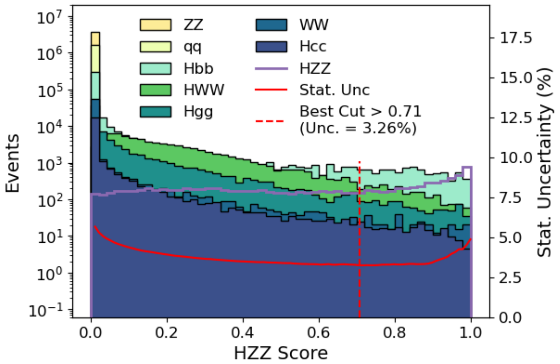

Figure 4. Score distributions and relative statistical uncertainties for $H \to b\bar{b}$, $H \to c\bar{c}$, $H \to gg$, $H \to WW^*$, and $H \to ZZ^*$ processes in the $\nu\bar{\nu}H$ analysis using the holistic approach trained on 100 k events. The purple curve denotes the signal, while the colored histograms show the backgrounds. The red solid curve gives the statistical uncertainty versus the score cut, and the vertical red dashed line marks the optimal score cut.

Our study incorporates only the Higgs-strahlung process. Including the WW-fusion process would result in an approximately 17% increase in the cross section for the $\nu\bar{\nu}H$ final state [8]. Taking this increase into account, and assuming for simplicity that the selection performance remains identical despite the kinematic differences introduced by the WW-fusion and interference effects, the relative statistical precision could be improved by roughly 9%. After scaling our results, these uncertainties achieve 0.16%, 0.86%, 0.43%, 0.39%, and 2.52%, respectively.

3.3. Extrapolate to Other Higgs Generation Modes

Table 4 summarizes the anticipated precisions of hadronic Higgs decay modes measurements using $\mu^+\mu^-H$ and $\nu\bar{\nu}H$ channels. Figure 5 compares these results with the projections from the CEPC Snowmass study [24] and recent FCC-ee estimates [13]. For the $H \to b\bar{b}$, $c\bar{c}$, and gg processes, the holistic approach yields significant improvements, reducing the relative uncertainties by a factor of approximately two to four compared to the Snowmass results. Remarkably, the precisions for these processes, together with $H \to WW^*$, are only 5% to 30% larger than the statistical limit. On the other hand, the $H \to ZZ^*$ process remains approximately a factor of two larger than the statistical limit, as it has a relatively small branching ratio and complicated event topology (see Appendix A).

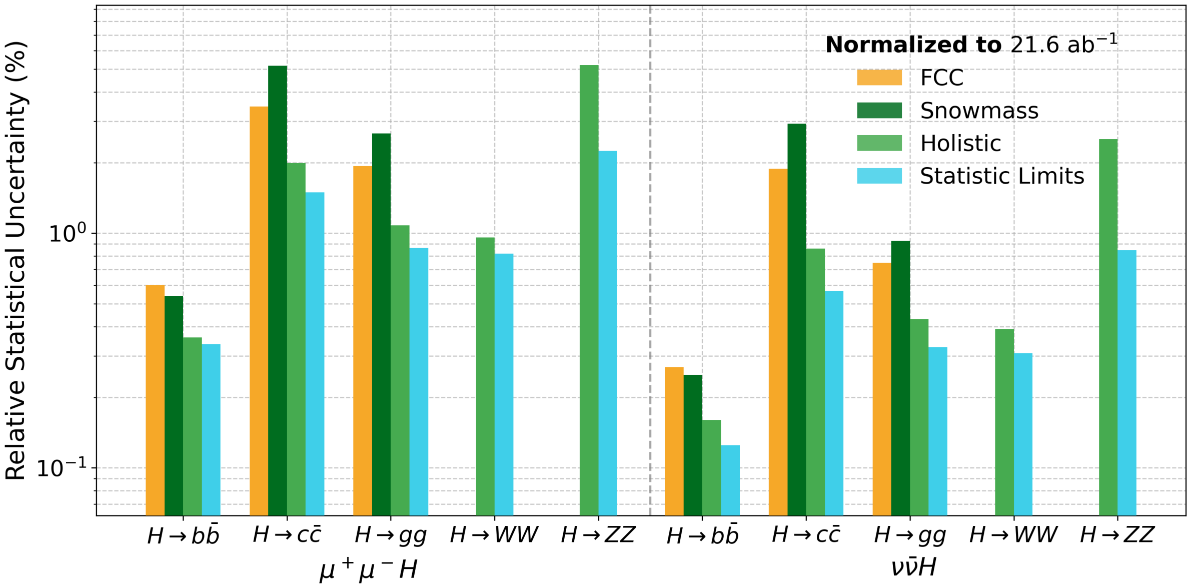

Figure 5. Combined precision for Higgs hadronic decay processes using the $\mu^+\mu^-H$ and $\nu\bar{\nu}H$ channels. The results obtained via the holistic approach are compared with the recent FCC-ee estimates [13] and the CEPC Snowmass 2021 baseline [24], where the specific $H \to b\bar{b}/c\bar{c}/gg$ results are taken from Ref. [17].

Table 4. Projected relative statistical precision for different Higgs hadronic decay processes with the integrated luminosity of 21.6 ab^{-1}. The results for $\mu^+\mu^- H$ and $\nu\bar{\nu}H$ are derived from the holistic analysis presented in this work, with the $\nu\bar{\nu}H$ precision scaled to account for the unsimulated WW-fusion production. The channels marked with an asterisk (*) are extrapolated estimates: The estimation assumes $q\bar{q}H$ achieves comparable precision to $\nu\bar{\nu}H$, while electron and tau channels are projected from the muon channel assuming a 10% cumulative performance degradation at each step.

Processes	$H\to b\bar{b}$	$H\to c\bar{c}$	$H\to gg$	$H\to WW^*$	$H\to ZZ^*$
$\mu^+\mu^- H$	0.36%	1.99%	1.08%	0.96%	5.21%
$\nu\bar{\nu}H$	0.16%	0.86%	0.43%	0.39%	2.52%
$e^+e^- H^*$	0.40%	2.19%	1.19%	1.06%	5.73%
$\tau^+\tau^- H^*$	0.44%	2.41%	1.31%	1.16%	6.30%
$q\bar{q}H^*$	0.16%	0.86%	0.43%	0.39%	2.52%

To provide a rough but complete preview, Table 4 also extrapolates these results to the other three Higgs production channels:

- $q\bar{q}H$ channel: We assume the sensitivities of those five Higgs hadronic decay modes from the $q\bar{q}H$ channel match those of the $\nu\bar{\nu}H$ channel (Precise measurements in the $q\bar{q}H$ channel require correctly grouping final-state particles originated from different bosons. To address this challenge, we propose Advanced Color Singlet Identification (ACSI) [16], implemented with a Transformer-based architecture. This AI-based method reduces the mis-grouped energy ratio by a factor of 3–5 and improves the expected sensitivity of $q\bar{q}H,\ H\to c\bar{c}/gg$ measurements to a level comparable to that of the $\nu\bar{\nu}H$ channel.). The $q\bar{q}H$ channel constitutes the majority of ZH events and has a statistics that is approximately three times larger than that of the $\nu\bar{\nu}H$ events. Meanwhile, precisely extracting Higgs property information from $q\bar{q}H$ events requires efficient identification of the Higgs decay products, which is a challenging task in fully hadronic events. In classical approaches relying on jet clustering and matching, the misidentification between Higgs and Z decay products is essentially the bottleneck for these measurements. Empowered by AI, the ACSI [16] has been developed recently, which reduces the error rate by a factor of four to five compared to the classical alternative. Therefore, considering that the combinatorial grouping bottleneck could be solved, the hadronic measurements could match or even exceed those of the $\nu\bar{\nu}H$ channel.
- $e^+e^- H$ channel: We derive the projection for the $e^+e^- H$ channel from the $\mu^+\mu^- H$ baseline by assuming a 10% degradation. On the signal side, the $e^+e^- H$ is about 7% more abundant than that of $\mu^+\mu^- H$, as the Z fusion process also leads to the $e^+e^- H$ final states; meanwhile, the background is also significantly higher than that of the $\mu^+\mu^- H$ channel, as a pattern of the electron-positron collisions. The reconstruction of $e^+e^- H$ is also less favorable compared to $\mu^+\mu^- H$ as the electrons radiate hard, while the advanced reconstruction could ameliorate these effects. Therefore, we assume a slight degradation compared to $\mu^+\mu^- H$.
- $\tau^+\tau^- H$ channel: We apply an additional 10% degradation relative to the electron channel projection. The signal and background yields of $\tau^+\tau^- H^*$ are well comparable to $\mu^+\mu^- H$, while the identification of τ is certainly a bit more challenging than the μ. A previous study shows that the τ reconstruction performance at $q\bar{q}H, H\to\tau^+\tau^-$ events (with quite similar topology to $\tau^+\tau^- H, H\to jj$) reaches an effective efficiency and purity of 80% [25], we estimate the performance degradation accordingly, while in fact, the τ reconstruction performance could be significantly improved by advancement in reconstruction especially those empowered by AI.

This study ignores the interference effects for simplicity (The interference will alter the yields of both signal and backgrounds. For the signal side, the signal yields of $e^+e^- H$ and $\nu\bar{\nu}H$ processes will increase by including ZZ and WW fusion and the relevant interference, where the yield change of the $\nu\bar{\nu}H$ channel has been taken into account in this manuscript. The background statistic could be altered, especially for the four-fermion background, i.e., $uudd$, which can come from both WW or ZZ processes or via its interference. Meanwhile, giving the efficient signal and background separation with a holistic approach, the typical S/B is significantly larger than one for the Higgs measurements in this manuscript, and thus, the anticipated accuracy is actually dominated by the signal statistic. Assume a relative change of SM background yields up to 10%, the consequent change of anticipated accuracy is limited to percentage level, thus we ignore this effect for simplicity.), not only in the signal channel (as the WW-fusion could lead to the same $\nu\bar{\nu}H$ final state interfering with $Z(\nu\bar{\nu})H$ events) but also in the background channels, where the four-fermion processes could interfere with each other. Meanwhile, as the Higgs signal could be efficiently separated from the backgrounds as demonstrated, the impact on the measurements of those leading Higgs modes should be small. These results account only for the statistical uncertainties, while the control of systematic and theoretical uncertainties is critical. In general, the systematic uncertainties of those Higgs measurements could, in principle, be controlled by the Z boson measurements, given the fact that CEPC could produce six orders of magnitude more Z bosons compared to the Higgs boson. The relevant systematics on detector performance (acceptance, efficiencies, differential resolution, and identification power) could, in principle, be controlled. Meanwhile, the one-to-one correspondence approach [15] also provides a mechanism to better monitor and calibrate the detector. It should be remarked that, as the holistic approach significantly improves the anticipated accuracies, the control of relevant systematic uncertainty becomes more challenging. For instance, as the $H \to b\bar{b}$ reaches per-mille level accuracy, the systematic uncertainty on luminosity measurements becomes comparable to the statistical error. Thus, the previous target of 10^{-3} for luminosity needs to be further improved. Another key component of the systematic uncertainty involves the calibration and robustness of the method itself, which is partly addressed by analyzing the scaling behavior and generator dependence in Section 4. While a comprehensive evaluation of systematic effects is beyond the scope of this study, we acknowledge that achieving the ultimate experimental precision will critically depend on the rigorous control of these systematics in future analyses.

4. Scaling Behavior

We observe that better performance can be achieved by increasing the training data size, echoing the well-known scaling law at Large Language Models (LLMs) [26,27]. We define the performance evolution as the scaling behavior, which characterizes the model's behavior at different tasks of scientific numerical processing. As a characteristic pattern, the scaling behavior is then applied to optimize the analysis, to monitor the AI model, and to control the relevant systematics.

4.1. Signal Efficiencies and Misidentification Rates

We evaluate the classification capability of the model as a function of training statistics, varying the dataset size from 1 to 10^6 events. Figure 6 illustrates the evolution of overall accuracy, which corresponds to the average trace of the row-normalized migration matrix, as well as the signal efficiencies, and specific misidentification rates for the $\mu^+\mu^- H$ channel.

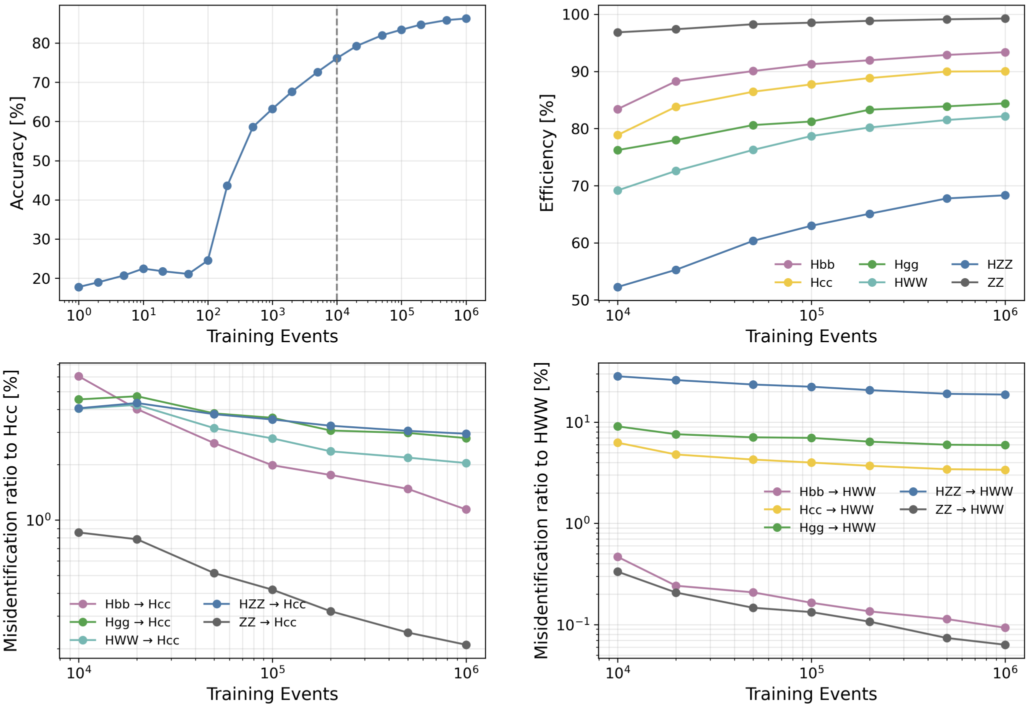

Figure 6. Top left: Overall accuracy as a function of training dataset size for the $Z(\mu^+\mu^-)H$ channel. **Top right**: Signal efficiency for each decay process versus training dataset size for the $Z(\mu^+\mu^-)H$ channel. **Bottom left**: Misidentification rate into the $H \to c\bar{c}$ channel versus training dataset size. **Bottom right**: Misidentification rate into the $H \to WW^*$ channel versus training dataset size.

As shown in the top-left panel of Figure 6, the overall accuracy, defined as the average value of the diagonal elements of the migration matrix, displays a typical S-curve dependence on the training data size. The learning trajectory can be conceptually divided into three distinct phases:

- Trivial phase: Near-random classification until the first critical point, corresponding to roughly 100 events.
- Rapid improvement phase: Performance improves rapidly with increasing data size, until roughly 10^5 events.
- Slow increase phase: a slow improvement phase in which the accuracy asymptotically approaches its limit. At the maximum available statistics of 10^6 events, the accuracy reaches approximately 86%.

The diagonal and off-diagonal elements of the migration matrix are extracted and presented, at training data sizes from 10^4 to 10^6. The signal efficiency curves (top-right panel) demonstrate distinct scaling behaviors across different Higgs decay processes. The vector boson decays ($H \to WW^*, H \to ZZ^*$) exhibit the steepest improvement slopes, indicating that larger datasets are particularly effective for identifying these four-jet topologies. In parallel, the heavy flavor modes ($H \to b\bar{b}, H \to c\bar{c}$) show a steady and consistent improvement, with the $H \to c\bar{c}$ accuracy increasing by approximately 10∼15%. Conversely, the $H \to gg$ channel displays a comparatively moderate improvement slope relative to the vector boson processes. These trends are consistent with the evolution of specific misidentification rates. As shown in the bottom-right panel, the misidentification of $H \to WW^*$ events as $H \to b\bar{b}$ or $H \to ZZ^*$ drops precipitously as the dataset expands. In contrast, the misidentification rates for the $H \to c\bar{c}$ channel (bottom-left panel) decrease more gradually, remaining the dominant source of background for the $c\bar{c}$ channel even at the highest statistics point.

4.2. Asymptotic Behavior of Anticipated Accuracies

Building on the classification performance, we model the dependence of the physics measurement uncertainty ($\delta\mu/\mu$) on the training dataset size. We employ a power-law ansatz with an irreducible term:

$$y = aN^{-\alpha} + c \tag{1}$$

Here, α denotes the scaling exponent governing the improvement rate, and c represents the asymptotic uncertainty floor, which corresponds to the irreducible confusion arising from the kinematic overlap between the signal and background phase spaces. Applying this scaling model to the $\mu^+\mu^-H$ channel, as shown in Figure 7, the precision improves significantly with increasing statistics.

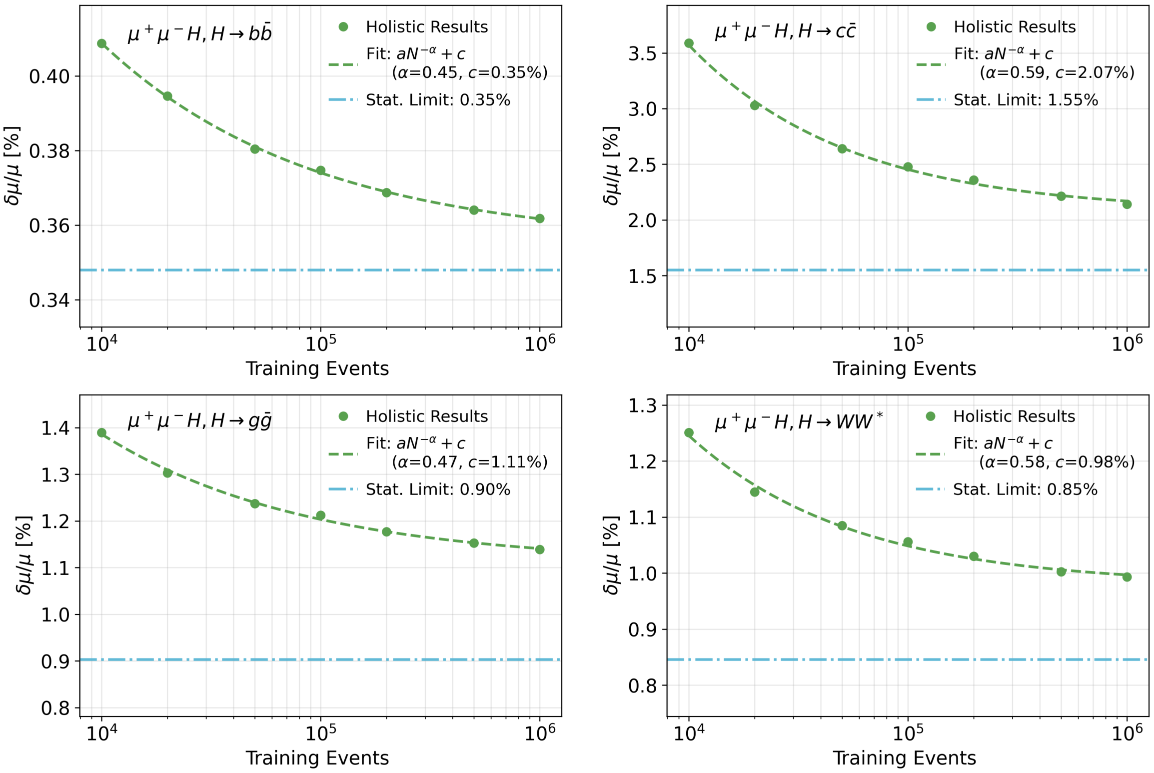

Figure 7. *Cont.*

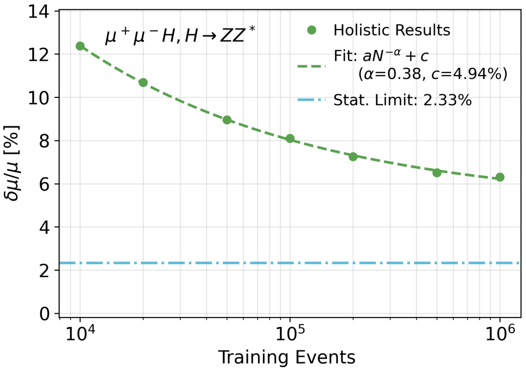

Figure 7. Scaling of measurement statistical uncertainty with training dataset size for the $Z(\mu^+\mu^-)H$ channel.

Two different asymptotic behaviors are observed for different decay processes. For $H \to b\bar{b}$, the projected precision asymptotically approaches the statistical limit. For other processes, especially $H \to ZZ^*$, a residual gap remains even at high statistics, suggesting the existence of a ceiling relevant to background misidentification.

4.3. Performance Dependence on Hadronization Models

The holistic approach utilizes reconstructed particles as input, which depend strongly on the parton fragmentation and hadronization models. This dependency is also relevant to the theoretical uncertainty. To analyze its impact, we perform a cross-validation using Herwig7 [28], which utilizes the Cluster fragmentation model [29], in contrast to the Lund String model [30,31] used by our training generator, Pythia8. We apply the models trained on Pythia8 datasets of varying sizes to an independent testing dataset generated with Herwig7.

Figure 8 presents the scaling of measurement precision for both generators.

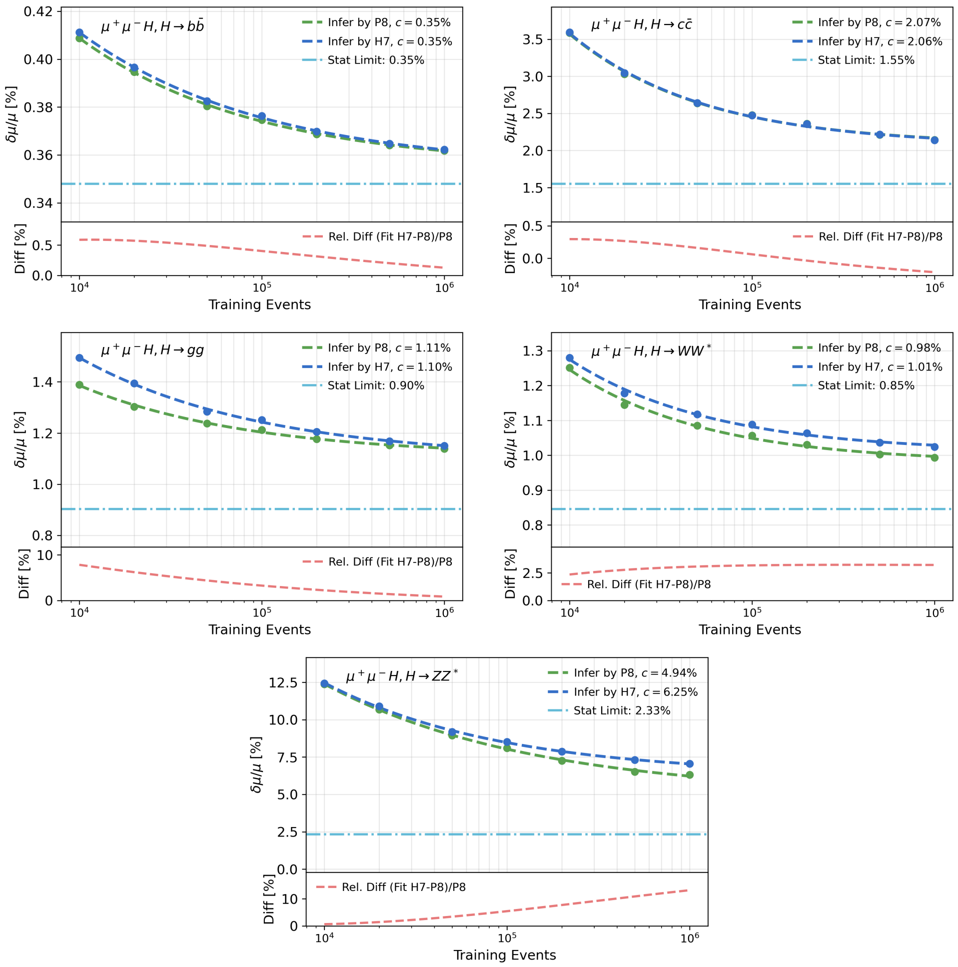

Figure 8. Scaling of measurement statistical uncertainty with training dataset size for the $Z(\mu^+\mu^-)H$ channel, comparing results with Herwig7 and Pythia8 inference.

The results show two distinct behaviors depending on the decay topology. For the two-body hadronic decays ($H \to b\bar{b}, H \to c\bar{c}, H \to gg$), the inference performance on Herwig7 samples shows a convergent trend relative to the Pythia8 baseline. As the training dataset expands toward 10^6 events, the measurement uncertainties derived from Herwig7 (blue lines) asymptotically approach or maintain a stable offset from the Pythia8 results (green lines). This suggests that for flavor tagging and gluon identification, increasing the training statistics allows the network to focus on robust features that are consistent across the Cluster and String fragmentation models.

In contrast, the four-body vector boson processes ($H \to WW^*, H \to ZZ^*$) exhibit a divergent trend. At low statistics (10^4 events), the performance gap between the two generators is minimal. However, as the statistics increase, the gap widens significantly: while the performance on the Pythia8 test set improves significantly with a steep slope, the improvement on the Herwig7 samples is more modest. As illustrated by the red curves representing the relative difference, the discrepancy increases with the training set size for these channels. This divergence indicates that for complex four-jet topologies, the network learns high-order kinematic correlations specific to the training generator (Pythia8) that do not fully generalize to the Herwig7 environment. Consequently, measurements of $H \to WW^*/ZZ^*$ will be subject to larger modeling systematic uncertainties compared to the two-body decay modes.

4.4. With/Without Pre-Selection

Figure 9 compares scaling behavior with and without pre-selection. It should be noted that due to the limited statistics of the surviving events after the rigorous pre-selection, the models in the "With Cut" scenario are trained on datasets of up to 10^5 events. The corresponding scaling curves are then extrapolated to 10^6 events using the fitted scaling law (Equation 1) to allow for a direct asymptotic comparison with the "Without Cut" scenario, which is trained on datasets up to 10^6 events.

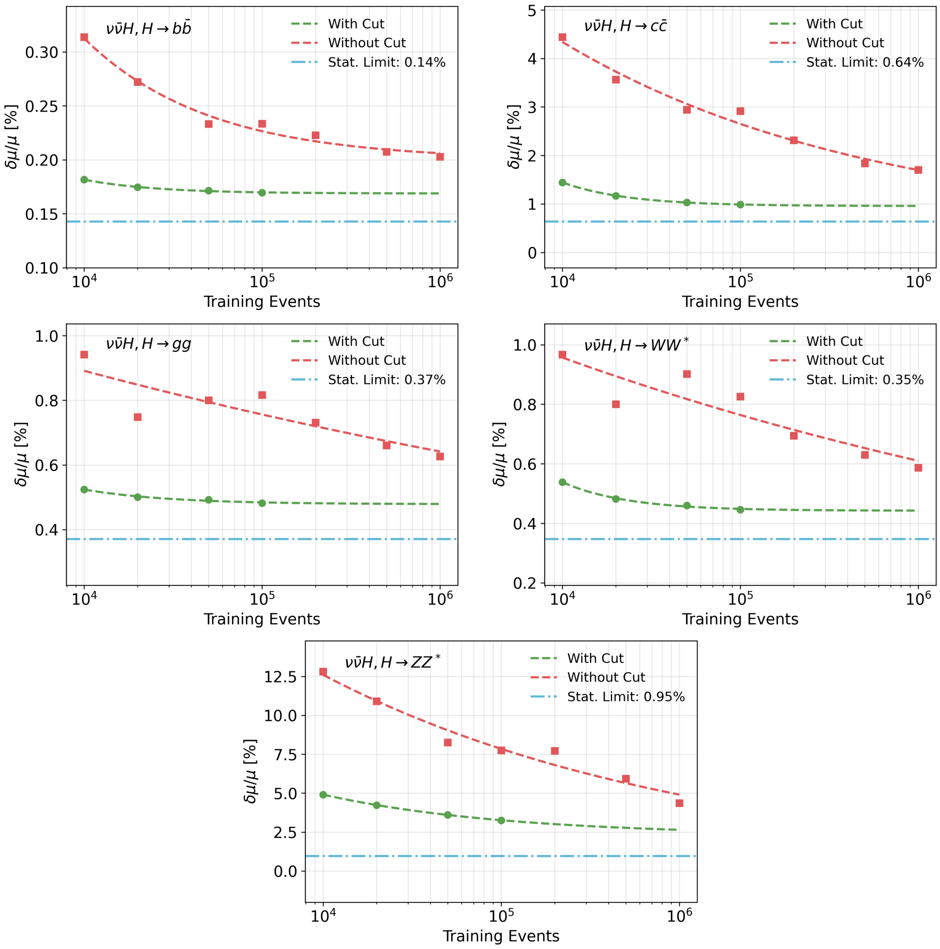

Figure 9. Scaling of measurement statistical uncertainty with training dataset size for the $Z(\nu\bar{\nu})H$ channel, comparing results with and without pre-selection. For the "with cut" scenario, the models are trained on datasets up to 10^5 events, and the curves extending to 10^6 events represent extrapolations based on the fitted scaling laws.

By using physics prior knowledge, pre-selection could strongly suppress the backgrounds at a certain cost to the signal efficiency, which becomes the ultimate ceiling of the final accuracy. Thus, an optimal analysis tactic needs to balance the strength of pre-selection and consequent holistic approach. We compare the scaling behavior of two tactics, "With Cut" and "Without Cut", corresponding to the analysis with and without pre-selection, see Figure 9. It shows that for small training data sizes, the "With Cut" configuration performs significantly better than "Without Cut", while the relative difference decreases as the training data size increases. Nevertheless, "With Cut" consistently outperforms "Without Cut" across all training data sizes. In other words, in the current realization, "Without Cut" needs tremendously more data to converge, and to surpass that of "With Cut". Therefore, to design better AI architecture with much faster convergence rates, and to better optimize the analysis tactic using physics prior knowledge, are critical topics to be explored in the future, especially for physics measurements with small signals and overwhelming backgrounds - those critical for discoveries.

5. Discussion and Summary

We estimate the accuracy of Higgs hadronic decay measurements at electron positron Higgs factory using the holistic approach, which identifies the physics process of each individual event by leveraging the inclusive information of reconstructed particles. Realized using a deep learning framework of PN, this approach yields two to four-fold improvement over the traditional cut-based methods at the CEPC. We analyze the scaling behavior of performance evolution with increasing size on the training data, which is then used to monitor and diagnose the deep learning performance, to optimize the analysis tactic, and to control the relevant uncertainties.

Applying holistic approach to the $Z(\mu^+\mu^-)H$ and $Z(\nu\bar{\nu})H$ processes with relevant Standard Model backgrounds, the anticipated relative statistical uncertainties for the $H \to b\bar{b}$, $c\bar{c}$, gg and $WW^* \to 4q$ measurements are 5% to 30% larger compared to the statistical limits. The $H \to ZZ^* \to 4q$ measurement is more challenging, as it has a relatively small branching ratio and complicated event topology, it is fragile to background processes, especially the irreducible ones of $H \to b\bar{b}$ and $H \to WW^*$ processes. By optimizing the analysis method, the anticipated accuracy of $H \to ZZ^*$ measurement can be improved by an additional 20% beyond the holistic approach results, eventually controlling the uncertainty to within a factor of two of the statistical limit. In other words, while the holistic approach is powerful due to the boosted dimensionality of the input information, incorporating physical prior knowledge is still appreciated in the current realization for those challenging measurements.

Based on the quantified accuracies of $\mu^+\mu^- H$ and $\nu\bar{\nu}H$ channels, we give a quick and rough estimation for all the other three Higgs generation channels. Certain simplifications were adopted to facilitate the estimation, and the corresponding limitations and relevant systematic uncertainties are discussed in Section 3.3. It should be remarked that the presented values could still be further improved. The observed scaling behavior indicates that better performance is possible with larger training datasets. While the currently anticipated accuracies, especially for the relatively more challenging channels like $H \to cc/gg/ZZ$, the improving trend is not fully saturated within the current algorithm architecture. Meanwhile, incorporating more information, for example, using the ACSI to better group the reconstructed particles, shall certainly be helpful for the $H \to ZZ$ and even $H \to WW$ measurements.

The holistic approach currently relies on supervised learning models. Its performance depends on the chosen AI architecture, the training procedure, and crucially, the data-MC discrepancy. The evolution of performance with increasing training data size, known as the scaling behavior, can be used to quantify relevant impact and diagnose AI behavior. As detailed in Section 4.2, the learning trajectory follows a typical S-curve, transitioning through a trivial near-random phase, a rapid improvement phase of feature extraction, and a slow increase phase where the anticipated accuracy asymptotically approaches its statistical limit. This scaling behavior is also used to quantify and optimize the analysis tactic. Comparing the learning curves shows that while physical pre-selection accelerates convergence at low statistics, the holistic approach might achieve better accuracies when the training data is sufficiently abundant and reliable. Furthermore, we analyze the scaling behavior on different pairs of hadronization models. As the training data statistic increases, the expected accuracies converge for different generator pairs for $H \to b\bar{b}$, $c\bar{c}$, gg measurements, while still exhibiting significant differences for $H \to WW^*$, ZZ^* measurements.

Leveraging the high-dimensional information contained in the input data and enabled by deep learning techniques, the holistic approach could significantly enhance the precision of key physics measurements and thus improve the discovery potential of Higgs factories. As an end-to-end framework, the holistic approach could, in principle, determine the signal and background simultaneously. In the current realization, however, analysis optimization guided by physics prior knowledge can still improve the performance, both in terms of output precision and computational cost. Another critical challenge for deep-learning-based methods is to quantify and control systematic and theoretical uncertainties, particularly those arising from data–MC discrepancies. In this context, the observed scaling behavior could serve as a useful diagnostic tool, providing valuable insight into the behavior of deep learning models.

Author Contributions

All authors have contributed to the publication, being variously involved in the conceptualization, simulation, data analysis, and paper writing and editing. All authors have read and agreed to the published version of the manuscript.

Funding

This research was funded by the National Key R&D Program of China, grant number 2024YFA1610603, and NSFC-funded International Collaboration Fund for Research teams W2441004.

Data Availability Statement

Not applicable.

Acknowledgments

We sincerely appreciate Tianji Cai for the helpful advice, and gratefully acknowledge Haijun Yang and Yanping Huang for their insightful discussions. We thank the HEPAI platform of the Institute of High Energy Physics for providing the computing resources.

Conflicts of Interest

The authors declare no conflict of interest.

Use of AI and AI-Assisted Technologies

No AI tools were utilized for this paper.

Appendix A. Categorization Strategy for the $H \rightarrow ZZ^*$ measurement

To improve the measurement precision, especially in the $H \rightarrow ZZ^*$ channel, we implement a categorization strategy that fully exploits the information of the holistic approach.

In Section 3.1, event selection relies on the signal itself's classification score to determine the optimal cut. But the misidentified score distributions also carry valuable information. For the $H \rightarrow ZZ^*$ channel, $H \rightarrow b\bar{b}$ and $H \rightarrow WW^*$ are the primary background. Therefore, we investigate the distribution of the inferred $H \rightarrow b\bar{b}$ and $H \rightarrow WW^*$ scores for the $H \rightarrow ZZ^*$ events.

The distinct double-peak structures are shown in the right panel of Figure A1. The lower score peak corresponds to events that share little topological resemblance to the respective background, while the higher score peak identifies events with features more akin to the background.

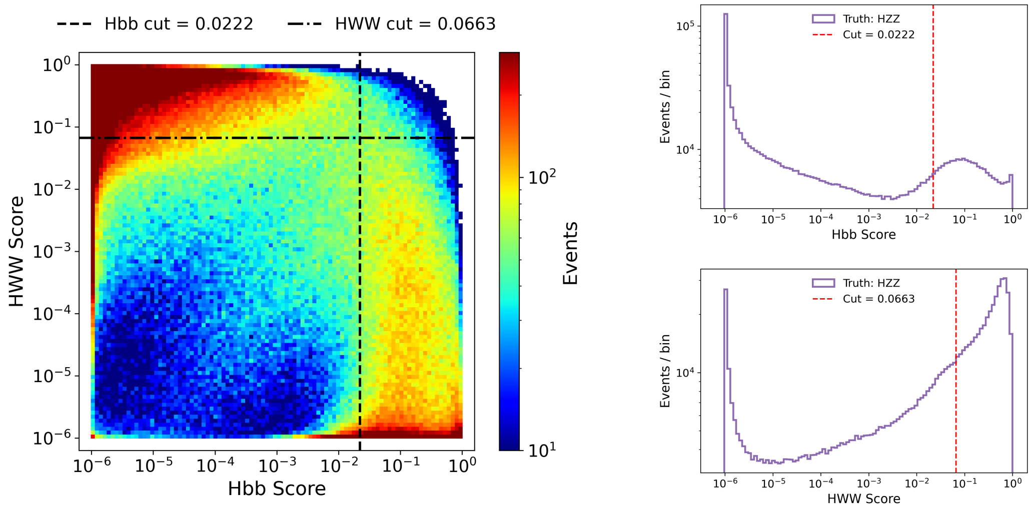

Figure A1. The left side of figure shows a 2D heatmap illustrating the joint distribution of the $H \rightarrow b\bar{b}$ score and $H \rightarrow WW^*$ score for $H \rightarrow ZZ^*$ events. The dashed lines indicate the dynamically optimized splitting boundaries. The right side of the figure shows the distributions of the inferred $H \rightarrow b\bar{b}$ score (top) and $H \rightarrow WW^*$ score (bottom) for the $H \rightarrow ZZ^*$ events.

To realize the separation, we analyze the joint 2D heatmap distribution of these two scores, shown in the left panel of Figure A1.

We divide the phase space into four distinct categories based on a set of orthogonal cuts applied to these two scores:

1. Low $H \to b\bar{b}$ and Low $H \to WW^*$
2. Low $H \to b\bar{b}$ and High $H \to WW^*$
3. High $H \to b\bar{b}$ and Low $H \to WW^*$
4. High $H \to b\bar{b}$ and High $H \to WW^*$

Within each of these four categories, we independently perform the same optimal cut method on the $H \to ZZ^*$ scores, as described in Section 3.1. Figure A2 shows the score distributions and the corresponding optimal cuts for these four regions.

The final measurement precision is obtained by statistically combining the uncertainties from these four regions. Because these regions are statistically independent, the combined relative statistical uncertainty (δ_{combined}) is calculated using the inverse sum of variances method, yielding the formula:

$$\frac{1}{\delta^2_{\text{combined}}} = \sum_{i=1}^{4} \frac{1}{\delta_i^2}$$

The exact splitting boundaries are determined dynamically by scanning the 2D score distribution to minimize the combined statistical uncertainty of the $H \to ZZ^*$ measurement. Applying this optimized categorization strategy yields a combined relative statistical uncertainty of 5.21%. This represents an approximate 20% improvement over the baseline result of 6.31% obtained from a single, global optimal cut.

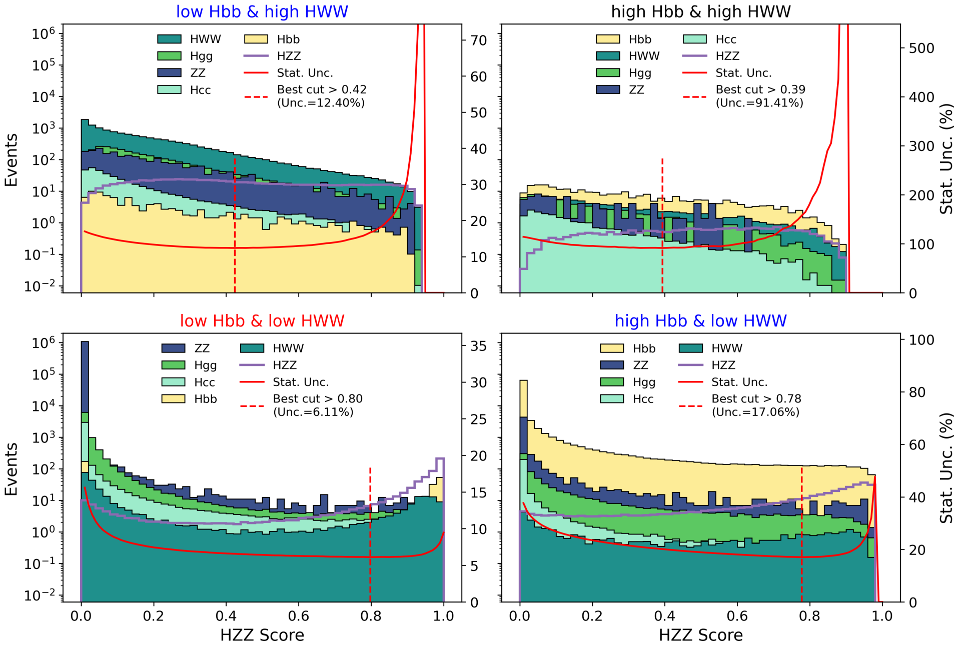

Figure A2. The $H \to ZZ^*$ score distributions and relative statistical uncertainties within the four isolated categories. The red solid curves represent the statistical uncertainty versus the score cut, and the vertical dashed lines mark the optimized thresholds for each independent region.

References

1. Aad, G.; Abajyan, T.; Abbott, B.; et al. Observation of a new particle in the search for the Standard Model Higgs boson with the ATLAS detector at the LHC. *Phys. Lett. B* **2012**, *716*, 1–29.
2. Chatrchyan, S.; Khachatryan, V.; Sirunyan, A.M.; et al. Observation of a New Boson at a Mass of 125 GeV with the CMS Experiment at the LHC. *Phys. Lett. B* **2012**, *716*, 30–61.
3. The European Strategy Group. *Deliberation Document on the 2020 Update of the European Strategy for Particle Physics*; Technical Report; CERN: Geneva, Switzerland, 2020.
4. de Blas, J.; Dunford, M.; Bagnaschi, E.; et al. Physics Briefing Book: Input for the 2026 update of the European Strategy for Particle Physics. *arXiv* **2025**, arXiv:2511.03883.

5. The CEPC Study Group. CEPC Conceptual Design Report: Volume 1—Accelerator. *arXiv* **2018**, arXiv:1809.00285.
6. The CEPC Study Group. CEPC Conceptual Design Report: Volume 2—Physics & Detector. *arXiv* **2018**, arXiv:1811.10545.
7. The CEPC Study Group. CEPC Technical Design Report: Accelerator. *Radiat. Detect. Technol. Methods* **2024**, *8*, 1–1105.
8. The CEPC Study Group. CEPC Technical Design Report—Reference Detector. *arXiv* **2025**, arXiv:2510.05260.
9. Agapov, I.; Benedikt, M.; Blondel, A.; et al. Future Circular Lepton Collider FCC-ee: Overview and Status. *arXiv* **2022**, arXiv:2203.08310.
10. Baer, H.; Barklow, T.; Fujii, K.; et al. The International Linear Collider Technical Design Report—Volume 2: Physics. *arXiv* **2013**, arXiv:1306.6352.
11. Linssen, L.; Miyamoto, A.; Stanitzki, M.; et al. Physics and Detectors at CLIC: CLIC Conceptual Design Report. *arXiv* **2012**, arXiv:1202.5940.
12. Anastopoulos, C.; Assmann, R.; Ball, A.; et al. LEP3: A High-Luminosity e^+e^- Higgs and ElectroweakFactory in the LHC Tunnel. *arXiv* **2025**, arXiv:2504.00541.
13. Del Vecchio, A.; Eysermans, J.; Gouskos, L.; et al. Precision Measurements of Higgs Hadronic Decay Modes at the FCC-ee. *arXiv* **2025**, arXiv:2511.23149.
14. Liang, H.; Zhu, Y.; Wang, Y.; et al. Jet-Origin Identification and Its Application at an Electron-Positron Higgs Factory. *Phys. Rev. Lett.* **2024**, *132*, 221802.
15. Wang, Y.; Liang, H.; Zhu, Y.; et al. One-to-one correspondence reconstruction at the electron-positron Higgs factory. *Comput. Phys. Commun.* **2025**, *314*, 109661.
16. Zhu, Y.; Liang, H.; Wang, Y.; et al. Holistic approach and Advanced Color Singlet Identification for physics measurements at high energy frontier. *arXiv* **2025**, arXiv:2506.11783.
17. Zhu, Y.; Cui, H.; Ruan, M. The Higgs$\rightarrow b\bar{b}$,$c\bar{c}$, gg measurement at CEPC. *JHEP* **2022**, *11*, 100.
18. Alwall, J.; Frederix, R.; Frixione, S.; et al. The automated computation of tree-level and next-to-leading order differential cross sections, and their matching to parton shower simulations. *JHEP* **2014**, *2014*, 79.
19. Frixione, S.; Mattelaer, O.; Zaro, M.; et al. Lepton collisions in MadGraph5_aMC@NLO. *arXiv* **2021**, arXiv:2108.10261.
20. Bierlich, C.; Chakraborty, S.; Desai, N.; et al. A comprehensive guide to the physics and usage of PYTHIA 8.3. *SciPost Phys. Codeb.* **2022**, *2022*, 8.
21. de Favereau, J.; Delaere, C.; Demin, P.; et al. DELPHES 3, A modular framework for fast simulation of a generic collider experiment. *JHEP* **2014**, *2014*, 57.
22. Qu, H.; Gouskos, L. ParticleNet: Jet Tagging via Particle Clouds. *Phys. Rev. D* **2020**, *101*, 056019.
23. Ma, X.; Wu, Z.; Wu, J.; et al. Measurements of decay branching fractions of the Higgs boson to hadronic final states at the CEPC. *Chin. Phys. C* **2025**, *49*, 053001.
24. Cheng, H.; Chiu, W.H.; Fang, Y.; et al. The Physics potential of the CEPC. Prepared for the US Snowmass Community Planning Exercise (Snowmass 2021). *arXiv* **2022**, arXiv:2205.08553.
25. Yu, D.; Ruan, M.; Boudry, V.; et al. The measurement of the $H \to \tau\tau$ signal strength in the future e^+e^- Higgs factories. *Eur. Phys. J. C* **2020**, *80*, 7.
26. Kaplan, J.; McCandlish, S.; Henighan, T.; et al. Scaling laws for neural language models. *arXiv* **2020**, arXiv:2001.08361.
27. Hoffmann, J.; Borgeaud, S.; Mensch, A.; et al. Training compute-optimal large language models. *arXiv* **2022**, arXiv:2203.15556.
28. Bewick, G.; Ravasio, S.F.; Gieseke, S.; et al. Herwig 7.3 release note. *Eur. Phys. J. C* **2024**, *84*, 1053.
29. Webber, B.R. A QCD Model for Jet Fragmentation Including Soft Gluon Interference. *Nucl. Phys. B* **1984**, *238*, 492–528.
30. Sjostrand, T. The Lund Monte Carlo for Jet Fragmentation. *Comput. Phys. Commun.* **1982**, *27*, 243.
31. Andersson, B. *The Lund Model*; Cambridge University Press: Cambridge, UK, 1998; Volume 7.